AGU PUBLICATIONS

Tectonics

RESEARCH ARTICLE
10.1002/2013TC003462

Key Points:
- InSAR shows postseismic afterslip at Sefidabeh occurring for over 16 years
- Geomorphology and InSAR estimates of topographic growth are in agreement
- Short-wavelength topography and geology can be produced by shallow afterslip

Correspondence to:
A. Copley,
acc41@cam.ac.uk

Citation:
Copley, A., and K. Reynolds (2014), Imaging topographic growth by long-lived postseismic afterslip at Sefidabeh, east Iran, *Tectonics*, *33*, doi:10.1002/2013TC003462.

Received 9 OCT 2013
Accepted 17 FEB 2014
Accepted article online 25 FEB 2014

Imaging topographic growth by long-lived postseismic afterslip at Sefidabeh, east Iran

Alex Copley[1] and Kirsty Reynolds[1]

[1]COMET+, Bullard Labs, Department of Earth Sciences, University of Cambridge, Cambridge, UK

Abstract This paper describes observations and models of the postseismic deformation following the 1994 Sefidabeh earthquake sequence in east Iran, which shed light on the nature of the earthquake cycle and the mechanisms of topographic growth in the region. Interferometric synthetic aperture radar observations show creeping fault motion ("postseismic afterslip") on an array of faults. Some of these faults probably represent the extensions of those that ruptured in the blind thrust-faulting earthquakes in 1994, and cut through the entire seismogenic layer, while others are shallow and break up the hanging walls of the coseismic faults. The postseismic slip accommodates at least part of the vertical displacement gradient resulting from the buried coseismic slip, which was concentrated at depths of greater than ~5 km. The postseismic afterslip is visible for over 16 years following the earthquakes. Agreement between the areas of postseismic uplift and indications of long-term motion preserved in the geomorphology suggest that shallow fault slip during seismic cycles similar to the one we have observed governs the development of the landscape in the region. Slip on an array of shallow faults provides a mechanism for the development of short-wavelength topography and geological structures above active thrust faults and has important implications for the interpretation of shallow geological features produced in regions experiencing similar seismic cycles to that at Sefidabeh.

1. Introduction

This paper presents observations and models of the postseismic deformation following the February 1994 Sefidabeh thrust-faulting earthquake sequence in east Iran. In less than a week, five earthquakes with moment magnitudes between 5.5 and 6.2 and centroid depths between 5 and 10 km [*Berberian et al.*, 2000] occurred near the town of Sefidabeh, on a fault system with an estimated convergence rate of ~1.5 mm/yr [*Parsons et al.*, 2006]. No surface ruptures on thrust faults that could have generated the earthquakes were visible in the field, but discontinuous bedding-parallel slip was seen within the hanging walls of the coseismic faults [*Berberian et al.*, 2000]. This slip was discontinuous in a zone 9.5 km long and 20 m wide and located on the crest of a topographic ridge at Sefidabeh that runs parallel to the earthquake nodal plane strikes. The bedding planes that slipped were within isoclinally folded and vertically dipping Upper Cretaceous–Paleocene flysch and volcaniclastic rocks [*Berberian et al.*, 2000]. Interferometric synthetic aperture radar (InSAR) interferograms covering the coseismic period show a "bull's-eye" pattern of surface displacements [*Parsons et al.*, 2006], indicating that the dominant coseismic slip was buried at depth, consistent with the lack of primary surface faulting. Modeling of the coseismic InSAR data implies that coseismic slip was concentrated at depths of 5–10 km [*Parsons et al.*, 2006], in agreement with the centroid depths estimated using body wave seismology [*Berberian et al.*, 2000]. This estimated depth range does not completely rule out the presence of shallower slip, but suggests that any shallow slip that did occur was minor compared with the deeper slip at 5–10 km. The fault planes that slipped in the earthquakes were oriented NW-SE, and the slip was close to pure thrusting (the mechanisms are shown in black in Figure 1a). The large cumulative displacement resulting from the earthquakes (equivalent to a single M_w 6.5 event), the excellent coherence in InSAR results from the region [*Parsons et al.*, 2006], and the clearly visible geomorphological effects of active faulting [*Berberian et al.*, 2000] make this earthquake sequence an ideal candidate for studying the evolution of deformation and topography during the earthquake cycle.

One reason for studying the postseismic signal of the Sefidabeh earthquakes is to constrain the timing within the seismic cycle when geomorphic features and geological structures are produced. By comparing the coseismic and postseismic surface motions with the indicators of active deformation preserved in the landscape, it is possible to infer what deformation, at what time in the seismic cycle, produced these

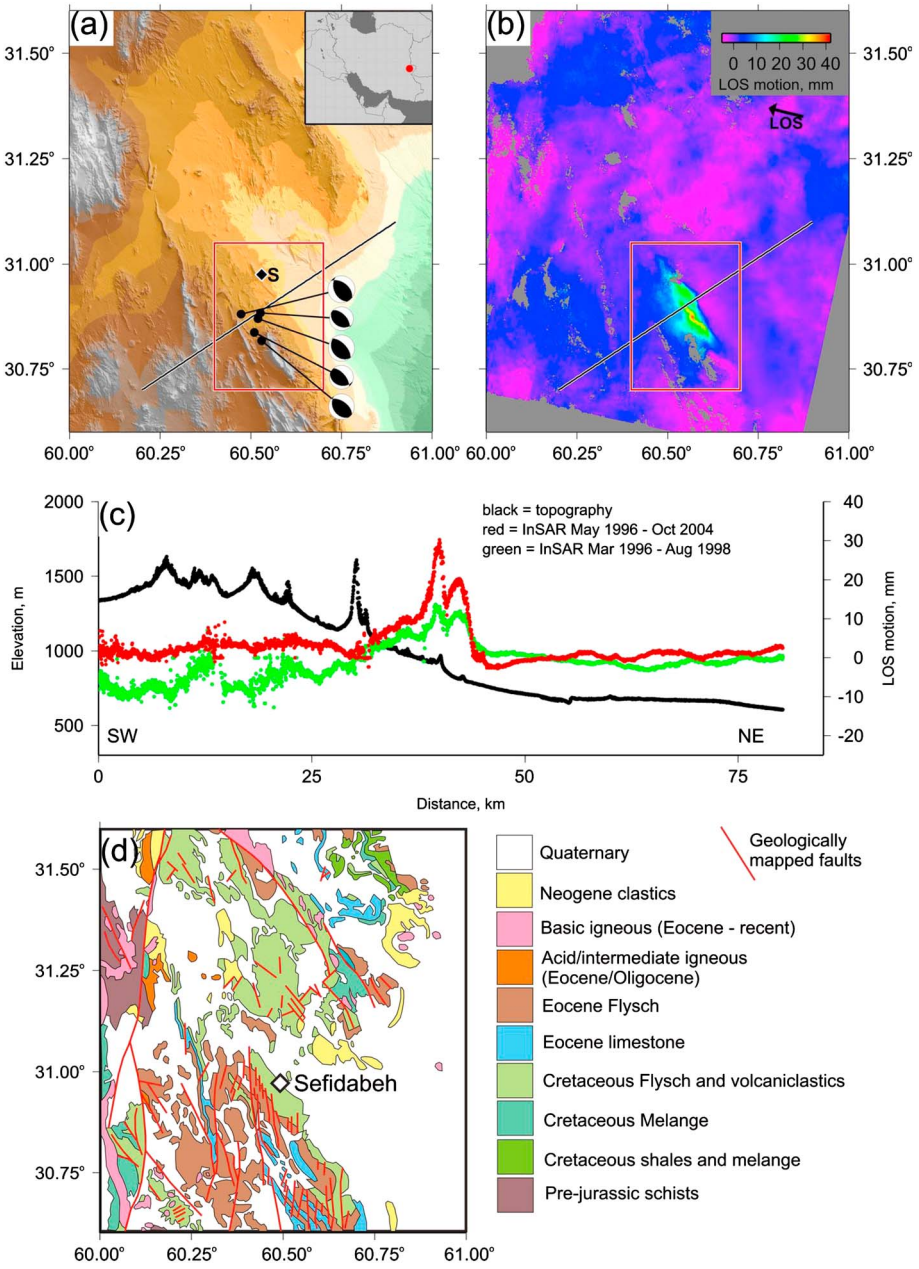

Figure 1. (a) Topography in the region of the Sefidabeh earthquake sequence (location shown in red on the inset map). The focal mechanisms represent the five events in the Sefidabeh earthquake sequence and are taken from *Berberian et al.* [2000]. The locations are taken from the relocations of *Parsons et al.* [2006]. The black diamond marked "S" shows the location of Sefidabeh village. (b) Postseismic InSAR interferogram covering the period May 1996 to October 2004, showing displacement in the line of sight (LOS) of the satellite, which is in the direction of the black arrow marked "LOS" and inclined at 23° to the vertical. Positive displacements correspond to motion toward the satellite. The red box shows the area of coverage of Figure 4. (c) Profiles of topography and InSAR line of sight displacement along the black lines in Figures 1a and 1b, projected from up to 200 m from either side of the line. The InSAR displacements are taken from the interferogram in Figure 1b (the red points) and one made with independent scenes covering the time period March 1996 to August 1998 (green points and shown in Figure 2a). The small, long-wavelength signal on the left side of the profile in green is likely to result from topographically correlated atmospheric effects. (d) Simplified geological map, adapted from the 1977 National Iranian Oil Company 1:1,000,000 sheet. Note that only major geologically mapped faults are shown and not some structures that have been revealed by recent active tectonic studies (e.g., those at Sefidabeh discussed here).

features (while acknowledging the possible role of slow, but long-term, interseismic creep). Such work has implications for understanding how the landscape evolves, for using geology and geomorphology to infer the characteristics of seismic cycles, and for estimating the material properties of faults and the surrounding lithosphere. Previous studies have also investigated the active deformation in zones of thrusting and its relation with the growth and evolution of geological and topographic structures. For example, *Yielding et al.* [1981] and *Philip et al.* [1992] discussed how the slip in the 1980 El Asnam and 1988 Spitak earthquakes resulted in the uplift of anticline ridges, accommodated by extensional faulting along the ridge crests. Elsewhere in Iran, *Fielding et al.* [2004] and *Nissen et al.* [2007] discussed the relationship between fault slip and shallow folding, and observed contrasting behavior of aseismic creep beneath a fold-thrust belt in eastern Iran, and coseismic slip that was only partially correlated with the surface folding on Qeshm Island in the Persian Gulf. A further style of behavior was seen following the 1999 Chi-Chi earthquake, where scarps were produced by active folding during the event [*Chen et al.*, 2007]. Given the variable behavior of these and other faults that have been studied, it is worthwhile to use the excellent InSAR coherence and clearly visible tectonic geomorphology to study the behavior of the Sefidabeh region following the 1994 earthquake sequence.

A feature that is commonly seen in continental thrust-faulting earthquakes is that fault slip decreases toward the surface or does not reach the surface (at Coalinga, Northridge, Bhuj, and San Simeon) [e.g., *Stein and King*, 1984; *Wald et al.*, 1996; *Copley et al.*, 2011; *Johanson and Burgmann*, 2010]. The same feature was seen at Sefidabeh, with slip concentrated at depths of 5–10 km [*Parsons et al.*, 2006]. A key question therefore concerns how this shallow deficit of slip is accommodated elsewhere in the seismic cycle, and how such deformation relates to the time-integrated behavior seen in the geological record of crustal shortening (as discussed below). The visible postseismic deformation signature, coupled with the previous work on the coseismic deformation [*Berberian et al.*, 2000; *Parsons et al.*, 2006], means that we can gain insights into this question by studying the Sefidabeh earthquake sequence.

A further reason for examining postseismic behavior and the growth of topography at Sefidabeh is due to the geology of the region. Previous studies have documented deformation and the evolution of geological and topographic structures in regions where thick sequences of relatively young and unconsolidated sediments undergo active shortening. Recent examples include studies of the pervasive deformation of thick piles of sediment on the margins of the Tien Shan and the Himalaya and in the Los Angeles Basin [e.g., *Allmendinger and Shaw*, 2000; *Lavé and Avouac*, 2000; *Scharer et al.*, 2006; *Daeron et al.*, 2007; *Charreau et al.*, 2008]. However, in contrast to these studies, the surface geology at Sefidabeh comprises volcanoclastics, flysch, and limestones that were deposited from the Cretaceous to the early Tertiary, at which time they were faulted and isoclinally folded [*Freund*, 1970; *Geological Survey of Iran*, 1991]. By comparing the deformation at Sefidabeh with that observed in the studies described above, it will therefore be possible to infer the effects of the shallow geological structure on the deformation and development of topography.

We will initially describe InSAR observations of postseismic displacements following the Sefidabeh earthquake sequence. We then present a model of the displacement field that can be used to constrain the deformation mechanism and geometry, and examine the temporal evolution of the motions. We also compare the postseismic surface displacements to the tectonic geomorphology in the region, in order to infer how the part of the seismic cycle we have observed compares with the longer-term tectonics of the area. Finally, we discuss the implications of our study of Sefidabeh for the growth and evolution of topography and geological structures in zones of thrusting.

2. Postseismic Surface Motions

We have measured surface displacements using InSAR from 2 to 16 years following the earthquake sequence (using data from the ERS and Envisat satellites on descending-track number 77). The interferograms were produced and unwrapped using the Caltech/JPL ROI-PAC software [*Rosen et al.*, 2004], and topographic signals were removed using the Shuttle Radar Topography Mission (SRTM) digital elevation model [*Farr and Kobrick*, 2000]. We made 11 interferograms using data from 10 acquisitions (details are given in Table 1). No phase ramps (which would result from orbital errors) were removed from the InSAR results, as there were no smoothly varying interferogram-wide signals that were of a comparable magnitude to the signal we discuss at Sefidabeh.

Table 1. Details of the Interferograms Used in This Study

Scene 1 Date (yyyy/mm/dd)	Scene 2 Date (yyyy/mm/dd)	Satellite	Track #	Perpendicular Baseline (m)	Duration (years)	Label (Figure 2)
1996/3/31	1998/8/23	ERS-2	77	222	2.4	a
1996/3/31	1999/7/4	ERS-2	77	297	3.3	b
1996/5/4	1996/5/5	ERS-1 and ERS-2	77	−108	0.003	c
1996/5/4	1999/5/30	ERS-1 and ERS-2	77	−152	3.1	d
1996/5/4	2004/10/10	ERS-1 and ERS-2	77	−32	8.4	e
1996/5/5	1999/5/30	ERS-2	77	−44	3.1	f
1996/5/5	2004/10/10	ERS-2	77	76	8.4	g
1998/8/23	1999/7/4	ERS-2	77	75	0.9	h
1999/5/30	2004/10/10	ERS-2	77	120	5.4	i
2003/11/30	2009/7/26	Envisat	77	−195	5.7	j
2003/11/30	2010/8/15	Envisat	77	−146	6.7	k

Figure 1 shows the topography in the region of the Sefidabeh earthquake sequence and the observed postseismic deformation over the time period May 1996 to October 2004 from a single interferogram (highlighting the excellent InSAR coherence in the region). The observed motion at Sefidabeh (up to 4 cm) is significantly higher than anywhere else in the interferogram. The signal is partially correlated with some small topographic features (ridges with up to ~100 m of local relief). However, we view the signal as tectonic in origin rather than being due to topographically correlated atmospheric effects for the following reasons. First, the signal is visible on multiple interferograms, made using independent data (see profiles in Figure 1, Table 1, and the interferograms and profiles in Figures 2 and 3). Second, the magnitude of the signal evolves with time in a consistent manner throughout our observation period, as will be discussed further below, and such a temporal pattern would not be expected from atmospheric signals. Third, the only place where such a signal is visible is where the Sefidabeh earthquakes occurred. Topographic features with similar characteristics, and also those spanning a large range of higher and lower wavelengths and amplitudes, are present throughout the area covered by the interferogram. However, none of these features have produced signals of greater than 15% of the amplitude of that seen at Sefidabeh in the interferogram shown in Figure 1. The profiles through two interferograms shown along with a topographic profile in Figure 1c, covering both the region of the Sefidabeh postseismic signal and also the surrounding area, highlight the high amplitudes of displacements seen at Sefidabeh compared to elsewhere in the interferogram (where topographic features are also present). Finally, although parts of the high-displacement patch correlate with topographic features, other parts do not (as will be discussed in more detail below), and the signal is continuous between the parts that are and are not correlated with the topography. The continuous nature of the signal (over both topographic ridges and valleys), the lack of correlation with the surface lithology, the sharp discontinuities present in the signal, the aridity of the region, and the presence of the signal in only the region of the Sefidabeh earthquakes, and not the geologically and climatologically similar areas along strike, lead us to also exclude hydrological effects such as aquifer filling or discharge as the source of the observed displacements. Note that some interferograms show a long-wavelength signal of up to ±5 mm in amplitude, for example in the profiles in Figure 3, at distances along the profiles of less than 4 km and greater than 20 km (the displacements between these points are part of the Sefidabeh signal that we study; see red profile in Figure 1c). However, this small long-wavelength signal effectively only changes the "base level" of the tectonic deformation at Sefidabeh, so interferograms that appear slightly different (e.g., Figures 2i and 2j) actually show very similar tectonic signals superimposed on this lower amplitude long-wavelength offset (Figure 3).

Data are also available from ascending-track ERS and Envisat acquisitions. However, less data were available than for descending-track number 77, and the available acquisitions meant that ~2.5 years was the longest interferogram that could be made. This interferogram only covers the northern part of the tectonic signal seen in the descending-track data. The sense of displacement (movement toward the satellite in region of the Sefidabeh earthquakes) is in agreement with the results from the descending-track data, consistent with thrust motion leading to a large component of vertical displacement. However, due to the short time frame of the interferogram (and the poor signal-to-noise ratio as a result), and the incomplete coverage of the Sefidabeh region, these data will not be considered further in this paper.

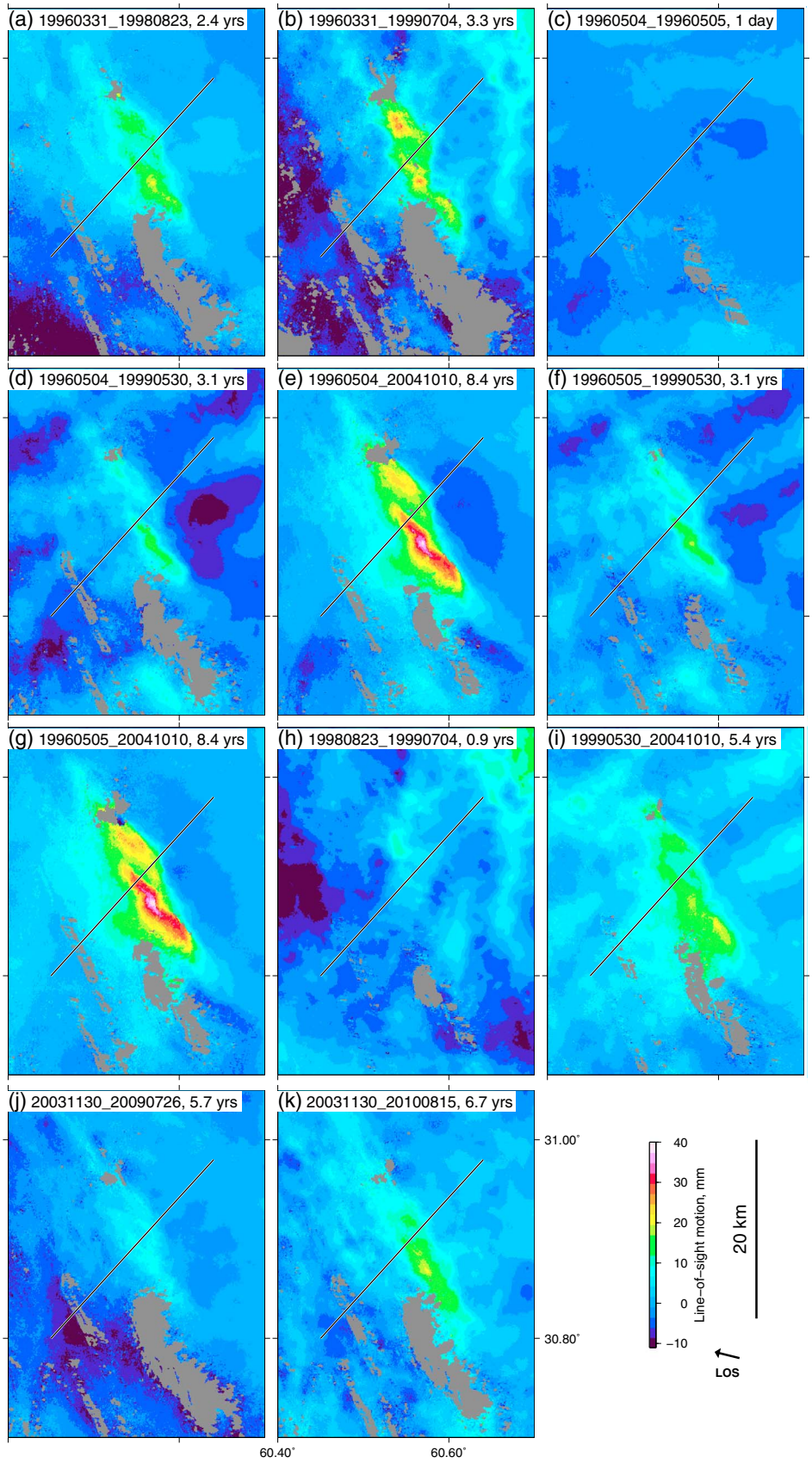

Figure 2

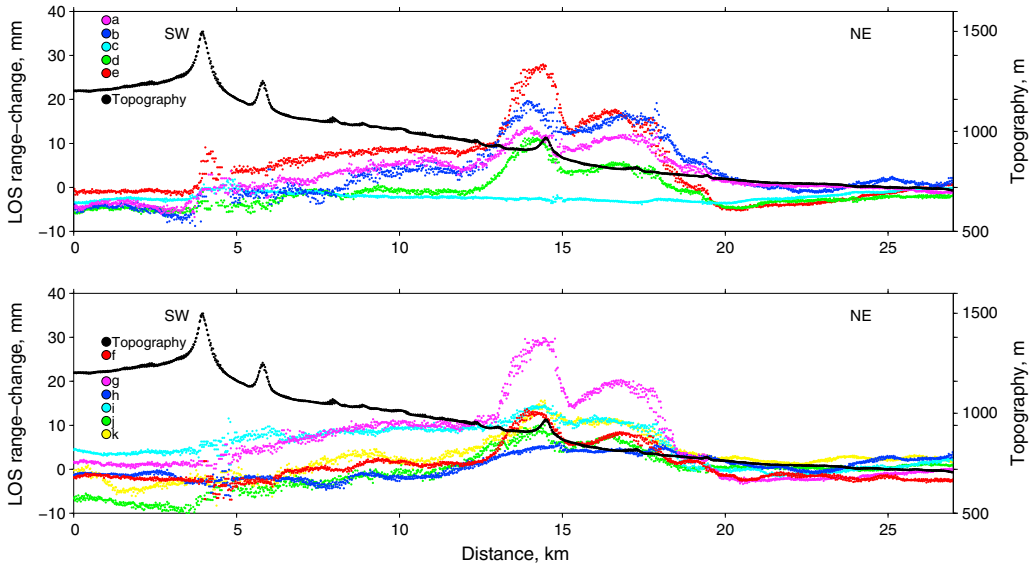

Figure 3. Profiles through the interferograms in Figure 2, along with the topography (separated onto two panels for clarity). The letters correspond to the subfigures of Figure 2 showing each interferogram. The blue line that shows no significant displacement as shown in Figure 2c is the 1 day interferogram. The profile location corresponds to the central section of that in Figure 1.

The evolution of the surface motions through time will be discussed in more detail below, but the most important feature to note at this stage is that there are two patterns present in Figures 2 and 3. First, the longer time period interferograms show the largest signals, such as Figures 2e and 2g, while the short-period interferograms show no features visible above the ±5 mm long-wavelength noise in the data, such as Figures 2c and 2h. Second, the rate of the displacements in the interferograms decreases through time, implying a decreasing rate of deformation. The signals in the shorter-time interferograms (e.g., Figures 2f and 2h) and in the ones later in the postseismic period (e.g., Figures 2j and 2k) therefore get smaller and approach the level of noise in the data, which leads to "smearing" of the displacement pattern. However, the signals are consistent enough in location, pattern, and magnitude to establish they are tectonic motion. Displacements are visible for our entire observation period, which finishes over 16 years after the earthquake sequence.

Figure 4 shows a larger-scale view of the observed surface motion. The interferogram spanning the coseismic period shows the smooth displacement pattern expected for buried slip that did not reach the surface [*Parsons et al.*, 2006]. Two years elapsed before the earliest postseismic SAR data were acquired (in 1996). The postseismic deformation field observed from 1996 onward is spatially complex. Multiple steep and narrow displacement gradients are present (Figures 4c, 4f, and 4g), with a range of strikes that are roughly NW-SE. The maximum satellite line of sight motion in the interferogram covering 1996–2004 is 4 cm, and over our entire 1996–2010 observation period is 6 cm. The incoherent area near Sefidabeh town at the northern part of the displacement patch corresponds to the location of uplifted lake beds. The linear incoherent areas further south correspond to steep topography on the edges of elongate topographic ridges.

The long timescale and spatially complex pattern of steep and narrow displacement gradients rules out poroelastic effects as the dominant cause of the signal. Likewise, the sharp displacement gradients rule out viscoelastic deformation or fault slip at depth as the dominant cause of the motions, as such mechanisms

Figure 2. (a–k) Interferograms of the Sefidabeh postseismic period. Labels represent the dates of the two Synthetic Aperture Radar (SAR) acquisitions used to make each interferogram, in the format yyyymmdd, and the time span of the interferogram. Ordering is according to date of first acquisition used, followed by increasing date of second acquisition. The line of sight of the satellite is in the direction shown by the arrow in the bottom right and inclined at 23° to the vertical. Positive values correspond to motion toward the satellite. Profiles through the interferograms shown in Figures 2a and 2g can be seen in Figure 1c, and profiles through all interferograms along the black lines in Figures 2a–2k are shown along with the topography in Figure 3.

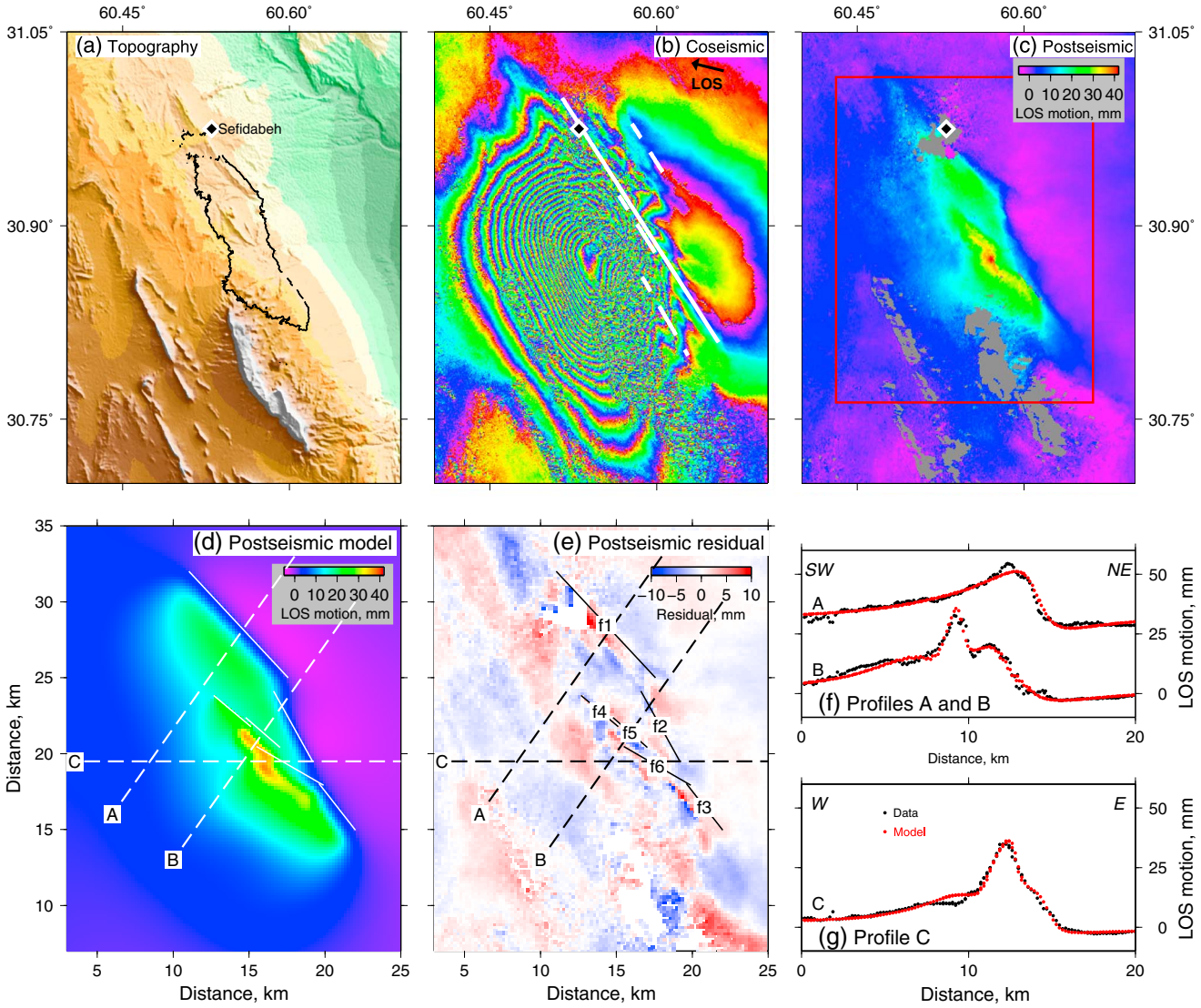

Figure 4. (a) Topography in the Sefidabeh region (location shown by the red box in Figure 1). The town of Sefidabeh is shown as a black diamond in Figures 4a–4c. The black line shows the contour of 15 mm motion in the postseismic interferogram shown in Figure 4c. (b) Coseismic interferogram covering October 1992 to May 1996 (each fringe represents 28.28 mm of ground motion in the line of sight (LOS) of the satellite, inclined at 23° to the vertical and in the azimuth marked by the black arrow). The maximum LOS motion, in the center of the displacement patch, is ~60 cm. This interferogram includes the first 2 years of the postseismic time period. The white solid line shows the surface projection of the fault plane *Parsons et al.* [2006] used to model the InSAR displacements, and the dashed lines show the same for their multiple-fault model. (c) Postseismic interferogram covering May 1996 to October 2004 (with the same line of sight as the coseismic interferogram). The red box outlines the area used for modeling the ground displacements. Positive displacements correspond to motion toward the satellite. (d) Dislocation model of the postseismic interferogram within the area enclosed by the red box in Figure 4c. White lines show the surface projections of the model fault planes. (e) Residual (calculated as model minus data) for the postseismic model in Figure 4d. (f and g) Data (black) and model prediction (red) along the profiles A, B, and C labeled in Figures 4d and 4e. Profile A has been offset by 30 mm for clarity.

would produce long-wavelength surface motions due to the presence of the elastic upper crust. However, the observations are consistent with slip on faults in the upper crust in the time following the earthquake sequence ("postseismic afterslip"). *Lyzenga et al.* [2000] noted that viscoelastic relaxation in the shallow crust, overlying a blind thrust fault, can produce the same pattern of surface deformation as afterslip on a shallow thrust fault. However, in the case they studied the deformation is smoothly varying at the surface, and the fault slip that could have generated the observations is buried. The presence of multiple steep and narrow displacement gradients at the surface in our postseismic observations at Sefidabeh rule out this form of deformation as the dominant postseismic strain. We therefore conclude that the displacements we have imaged are due to postseismic afterslip.

3. Postseismic Deformation Model

3.1. Inversion Method

We will initially analyze the spatial pattern of the deformation that occurred following the Sefidabeh earthquakes, using a single interferogram covering the time period May 1996 to October 2004 (Figures 1 and 2g). This interferogram was chosen because its long time span, starting early in the postseismic period, combined with the low levels of nontectonic signal in areas distant from the Sefidabeh postseismic motions, leads to an excellent signal-to-noise ratio. The noise level can be seen in the profile through the interferogram shown in red in Figure 1, in the regions away from Sefidabeh, and is less than 0.5 cm (compared with the 4 cm maximum signal in the interferogram). There is no indication that the spatial pattern of displacement in this interferogram differs from that in any others, once the effects of the nontectonic noise in the noisier interferograms is taken into account (Figure 2), meaning our results using this interferogram apply to the deformation in all of the postseismic time period that we have observed (of which this interferogram covers roughly two thirds). After analyzing the spatial pattern of the deformation, we will then consider the temporal evolution of the motions.

It is possible to invert the surface displacement field to estimate the fault geometry and slip at depth, using displacements calculated for slip on rectangular fault planes [*Okada*, 1985]. Because of the complexity of the surface deformation field, six fault planes are required to recreate the observations. We use an iterative inversion scheme to find the combination of location, geometry, and slip on rectangular uniform slip fault planes that best fits the data. We begin with a single plane and then add extra planes after each inversion run in the location that shows the biggest discrepancy between the model predictions and the data. The parameters of all planes are then reinverted. We vary the starting parameters of the additional fault planes between different sets of inversions, to include initial dips between 10 and 80° , lengths from 1 to 15 km, and initial rakes between pure left-lateral strike slip, thrusting, and pure right-lateral strike slip. We assess the quality of fit between the model and the data using the reduced chi-square statistic, which is given by $\chi^2_{\mathrm{red}} = \frac{1}{N}\sum\frac{(D-M)^2}{\sigma^2}$, where N is the degrees of freedom (number of observations minus number of model parameters minus one), D and M are the observed and modeled displacements at each point, σ^2 is the variance of the data (calculated from the regions of the interferogram not affected by the Sefidabeh postseismic motion), and the sum is over all model grid points. We assume the data variance in the region of the tectonic motions is the same as in the surrounding area of the interferogram. In cases where $\chi^2_{\mathrm{red}} = 1$, the misfit between the model and the data is the same size as the uncertainty in the data. Large values are equivalent to a poor fit to the data and values significantly less than one imply fitting of noise in addition to the signal present in the data (i.e., overfitting of the data). Our preferred model includes six fault planes (Figure 4d) and has $\chi^2_{\mathrm{red}} = 1.15$, implying that we are neither significantly underfitting or overfitting the data. A visual corollary of this point can be seen on the profile through the interferogram shown in Figure 1c, which gives a sense of the size of the tectonic signal (>30 mm on the section shown on the profile and ~40 mm at its maximum) in relation to the minor undulations in the other parts of the interferogram (<5 mm), showing that the signal we are fitting is large compared with the noise level and the complexity of our modeled surface displacement field is justified. Fewer fault planes result in a significantly larger χ^2_{red}, because of an inadequate fit to the data ($\chi^2_{\mathrm{red}} = 1.80$ for five fault planes). Visual confirmation of this result arises from the large and spatially broad misfits resulting from five fault models. Additional planes reduce the χ^2_{red} value only slightly (to 1.04), indicating that the main features of the data are explained with six fault segments.

3.2. Inversion Results

The level of noise in the data is low enough that we would be able to obtain well-constrained estimates of the parameters of a single fault plane. However, two other factors place constraints on the resolving power of our models. First, the only usable data we have are from a single descending-track look angle, so we are affected by some commonly known trade-offs between fault parameters. The second limiting factor in our inversions is that six closely spaced faults are required to fit the data. The overlapping surface displacement patterns due to these fault segments leads to trade-offs between the parameters of the faults. We have investigated the range of model parameters that provide a good fit to the data (i.e., with a χ^2_{red} comparably low as our preferred model described below) by varying the starting parameters of fault planes as they were added to the inversions. The combination of these two effects means that there are trade-offs between the magnitudes of slip, the rakes, and the dips of the fault planes. However, there are a number of robust features that are present in all fault configurations we have found that provide a good fit to the data, which are described below.

Table 2. Parameters of the Fault Model Shown in Figure 4d. *X* and *Y* Locations Correspond to the Position of the Surface Projection of the Along-Strike Center of the Fault Plane

Fault Label (Figure 4e)	*X* Location (km)	*Y* Location (km)	Strike (deg)	Dip (deg)	Rake (deg)	Slip (cm)	Length (km)	Top Depth (km)	Bottom Depth (km)
f1	14.3	28.5	137	61	90	4.5	9.6	1.3	8.5
f2	17.9	21.8	151	68	90	3.0	5.3	0.9	12.5
f3	20.8	16.5	142	40	85	5.0	3.9	0.9	10.0
f4	13.9	22.8	130	37	70	1.5	3.2	0.0	8.0
f5	15.9	21.4	131	28	60	5.0	3.0	0.4	1.0
f6	17.7	19.2	120	34	110	5.0	5.1	0.6	3.5

In our preferred model (shown in Figure 4d) the magnitude of slip on all the planes is 5 cm or less, and the faults have dominantly thrust motion with dips to the SW in the 28–68° range (the parameters of the fault model shown in Figure 4d are given in Table 2). Slip reaches within 1 km of the surface and in some cases breaks the surface, on the fault segments that underlie sharp displacement gradients. The long-wavelength component of the surface deformation (Figure 4c) requires slip on the three northeastern fault planes that lie along the range-front (f1–f3 in Figure 4e) to extend to a depth of 10 ± 3 km (e.g., fault f1 crossed by profile A in Figure 4f). The short-wavelength features present in the displacement field show that either two or all three of the faults within the range interior (f4–f6 in Figure 4e) only slipped at shallower depths (i.e., <5 km, such as fault f5 responsible for the short-wavelength displacement peak on profile B in Figure 4f). The total moment represented by the afterslip in the model shown in Figure 4d is 5×10^{17} Nm (equivalent to a single event of M_w 5.8). Three earthquakes of magnitudes 3.6–3.8 are the only to be present in the area in the International Seismological Centre (ISC) catalog during the time covered by our postseismic InSAR results, suggesting the deformation is likely to have been mostly aseismic (over 300 such events would have been required to produce the observed deformation). Our estimate of the magnitude of postseismic slip does not include the unobserved deformation in the 2 years immediately following the earthquake sequence or the displacements following the end date of the interferogram analyzed in this section of 2004.

It is likely that the slip from the near surface to depths of 10 ± 3 km on the range-front faults represents motion on the continuations of the coseismic fault planes, which *Parsons et al.* [2006] demonstrated would project to the surface near the range-front (marked in white in Figure 4b). Within the uncertainties in the fault location and dip estimates of *Parsons et al.* [2006] (due to decorrelated areas in their interferograms) and this study, the range-front faults in our model are consistent with being extensions of the same planes as the coseismic fault ruptures of *Parsons et al.* [2006]. The base of slip we estimated is similar to the ~10 km maximum depth of coseismic slip estimated by *Parsons et al.* [2006]. However, our estimated postseismic slip extends close to the surface rather than being buried at depths of >5 km as was the case coseismically. Both coseismic and postseismic slip was dominantly thrusting. These relations between coseismic and postseismic slip suggests that the postseismic motion was driven by stress concentrations on the edges of the coseismic rupture patch (a common occurrence) [e.g., *Johnson et al.*, 2006; *Hsu et al.*, 2006; *D'Agostino et al.*, 2012; *Copley et al.*, 2012]. The degree of sensitivity of our data to the detailed spatial distribution of motions at the 5–10 km depths of coseismic slip, and our use of rectangular constant slip fault planes in our inversions, does not allow us to infer whether there are gaps in the distribution of afterslip at depth that correspond to the fault patches that slipped in the earthquakes. However, because of its depth extent, the postseismic slip can be seen as a mechanism by which the vertical displacement gradient resulting from the buried coseismic slip is at least partly accommodated in the upper 5 km of the crust. The proportion of this displacement gradient accommodated by the afterslip will be discussed once the temporal evolution of the displacements has been examined.

There is no evidence of coseismic slip on faults within the interior of the range, southwest of the range-front thrusts just discussed (faults f1–f3). However, this region in the range interior experienced postseismic motion on shallow faults (<5 km, such as the fault f5 responsible for the short-wavelength displacement peak on profile B). It is possible that some coseismic slip in this region could have been obscured by the decorrelated patches in the coseismic interferogram (Figure 4b). However, such slip would also have had to be shallow, for the signal to have a short enough wavelength to be hidden within the decorrelated patch. Additionally, in order to be consistent with the 5–10 km centroid depths of the earthquakes determined using body waveform modeling [*Berberian et al.*, 2000], any slip would have had to be minor compared with

that at depth. It therefore appears that shallow postseismic slip, and possibly minor shallow coseismic slip that was unseen, occurred within the hanging walls of the range-front faults on which coseismic slip was concentrated and afterslip throughout the seismogenic layer later occurred.

4. Temporal Evolution of the Displacements

Unfortunately, the 2 year time gap between the earthquakes and the first postseismic SAR acquisition, the long gaps between subsequent data collections, and the increasingly poor signal-to-noise ratio in the later part of the observation period, limit our ability to analyze the temporal evolution of the deformation. The displacement rate is not constant, with the time-averaged rate at the highest-displacement locations decreasing from ~7 mm/yr in the period from 2 to 4.5 years following the earthquakes (e.g., Figure 2a), to less than 3 mm/yr in the period beyond 9 years following the earthquakes (e.g., Figure 2k). This decrease in rate implies that the fault slip is relaxing the coseismic stress changes, and we are not observing interseismic creep at a constant rate. Additionally, the long-term rate of convergence across the fault zone is estimated to be ~1.5 mm/yr (from the dating of uplifted lake deposits) [*Parsons et al.*, 2006]. Although the rates late in our observation period approach this value, they remain higher, and the early rate is significantly higher, therefore implying that the interseismic contribution to our observations is small compared with the transient and decaying postseismic deformation.

Perfettini and Avouac [2004] derived an equation to describe the evolution of surface displacement due to postseismic fault slip driven by coseismic stress changes, which is given by $U(t) = \alpha V_0 t + \beta V_0 t_r \log[1 + d(\exp(t/t_r) - 1)]$, where $U(t)$ is the surface displacement through time, V_0 is the interseismic rate, t_r is the characteristic relaxation timescale of the deformation, α and β are geometrical factors, and d is a quantity that depends upon the coseismic stress change and the material properties of the fault plane. We do not have a complete enough time series of data, especially close to the time of the earthquakes, to be able to uniquely constrain the values of the parameters in this equation. We are therefore not able to estimate the material properties of the fault planes. Although the time-averaged rate of motion is known from the slip rate estimate of *Parsons et al.* [2006], the progressively decreasing rate of motion we have observed, and the rapid rates compared to the interseismic rate, mean that the signal is dominated by the postseismic transient deformation throughout our observation period, and knowledge of the time-averaged rate alone does not provide significant constraints upon the range of model parameters. However, it is still possible to place some constraints on the relaxation time (t_r). We have fixed the relaxation time at successive values and sought the combinations of the other parameters that result in an evolution of surface motions through time that best fit the interferograms shown in Figure 2. We have then examined how the misfit between the best fitting models and the data varies as a function of the relaxation time, as shown in Figure 5a. This method constrains the relaxation time to be greater than 4 years, assuming a noise level in the data of ±5 mm (from the noisiest interferograms, e.g., Figure 2d and 2f, which show a NE-SW trending artifact relating to the SAR data gathered in May 1999). The upper bound on the relaxation time is unconstrained, given the noise level in the interferograms.

The timescale of afterslip at Sefidabeh is considerably longer than is usually observed (0.1–1 years) [e.g., *Savage et al.*, 2005], as was also seen following the nearby 1978 M_w 7.3 Tabas earthquake [*Copley*, 2014]. In this case, *Copley* [2014] suggested two possible reasons for the long timescale, both of which could be applicable to the Sefidabeh postseismic slip. One possibility is that the fault has similar material properties to others that have been studied, but that the excellent InSAR coherence and the absence of other signals in the data (including interseismic motions, nontectonic effects, and other noise in the data) make small and long-lived signals more visible than may have been the case following other earthquakes. Both the 1978 Tabas event and the M_w 9.2 1964 Alaska earthquake [*Suito and Freymueller*, 2009] produced afterslip on longer time frames than has happened to date at Sefidabeh (although the motions are likely to still be continuing). An alternative possibility is that there is significant lateral variability in the material properties of fault planes, and therefore the time periods over which they experience postseismic afterslip. Relatively short transients following other events [e.g., Loma Prieta, Denali, and Mozambique; *Segall et al.*, 2000; *Johnson et al.*, 2009; *Copley et al.*, 2012] suggest that some variability does exist, but at present we do not have sufficient information to establish which of these two possibilities is responsible for the observations presented in this paper.

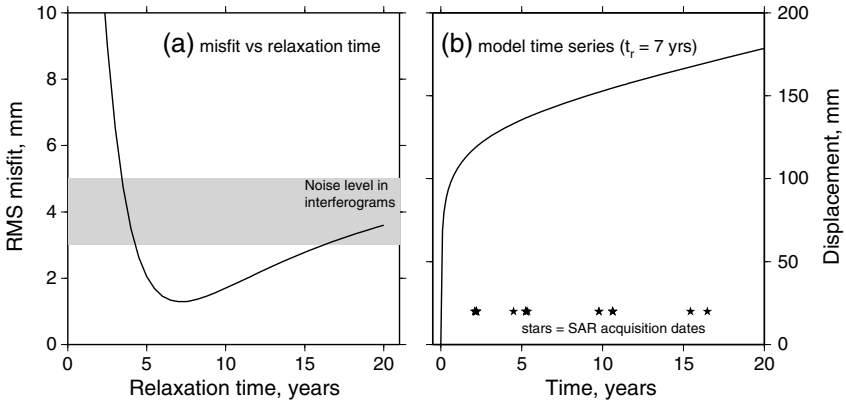

Figure 5. (a) Plot of misfit between the InSAR data and a model for afterslip driven by coseismic stress changes (calculated from the expressions of *Perfettini and Avouac* [2004]), as a function of the characteristic relaxation time. The noise level in the interferograms ranges between ~3 and ~5 mm/yr and is shown by the grey bar. The shape of the misfit curve means that significant changes in the noise level of the interferograms would be required in order to change our ability to resolve the relaxation time. (b) Sample model prediction for a relaxation time of 7 years. The black stars show the dates of SAR acquisitions.

For the best fitting models corresponding to the low misfits in Figure 5a, the total surface motion at the maximum displacement point in the 20 years following the earthquakes is estimated to be 0.1–0.2 m (Figure 5b). Adding up the motion across strike on the range-front and hanging wall faults, this displacement corresponds to a total of 0.25–0.5 m shallow fault slip per length along strike. Such shallow slip represents 13–25% of the magnitude of deep coseismic slip and therefore the same proportion of the displacement contrast between the coseismic slip patch and the unruptured upper ~5 km of the crust. However, the trade-offs amongst the parameters mean this estimate cannot be refined any further using the available data. The large uncertainty mostly relates to our lack of data from the first 2 years following the earthquakes, when the rates would have been higher and most slip would have occurred (Figure 5b). The component of the vertical displacement contrast produced by the buried earthquake slip that is not accommodated by the postseismic slip we have studied is likely to be relieved by future long-lived postseismic motion or interseismic creep.

5. Relationship to Geomorphology

The deformation observed in the postseismic InSAR results is in direct agreement with geomorphological indicators of the location of active uplift. The abandoned and incised alluvial fan surfaces described by *Berberian et al.* [2000] mark the locations of uplift on timescales of multiple seismic cycles and are in agreement with the areas of postseismic uplift. Growing ridges within the mountains have diverted rivers around their ends [*Berberian et al.*, 2000], and these ridges are locations of concentrated postseismic uplift. Figure 6 highlights the spatial agreement between the geomorphological signs of long-term uplift of ridges and the diversion of drainage, and the motion observed in the postseismic InSAR results (e.g., the two areas marked "A" and "B"). A third sharp displacement gradient in the InSAR results, marked "C" in Figure 6c, does not coincide with a topographic ridge, but does mark a region of significant incision of alluvial fans. Elevation data (Figures 1a, 1c, and 6d) show that the faults whose slip we have inferred based on the InSAR results have not been responsible for producing all of the topography in the region, some of which presumably relates to earlier phases of faulting or volcanism, plus erosion (e.g., the 50 km long SW-NE gradient that crosses the area). However, the geomorphological markers of uplift on shorter timescales (e.g., tens to hundreds of thousands of years), such as the diversion and incision of drainage and the growth of the ridges close to the range-front that have uplifted ~100 ka age lake deposits [*Parsons et al.*, 2006] are in agreement with the locations of motion in the postseismic InSAR results. Such features are too narrow to have been produced by smooth, long-wavelength, coseismic uplift during earthquakes similar to those in 1994 (Figure 4b). The agreement between the uplift patterns in the postseismic motion and the geomorphology is important because it suggests that the Quaternary landscape development in the region is governed by seismic cycles of the type that we have observed. An understanding of these observations can therefore provide insights into the development of topography in the area.

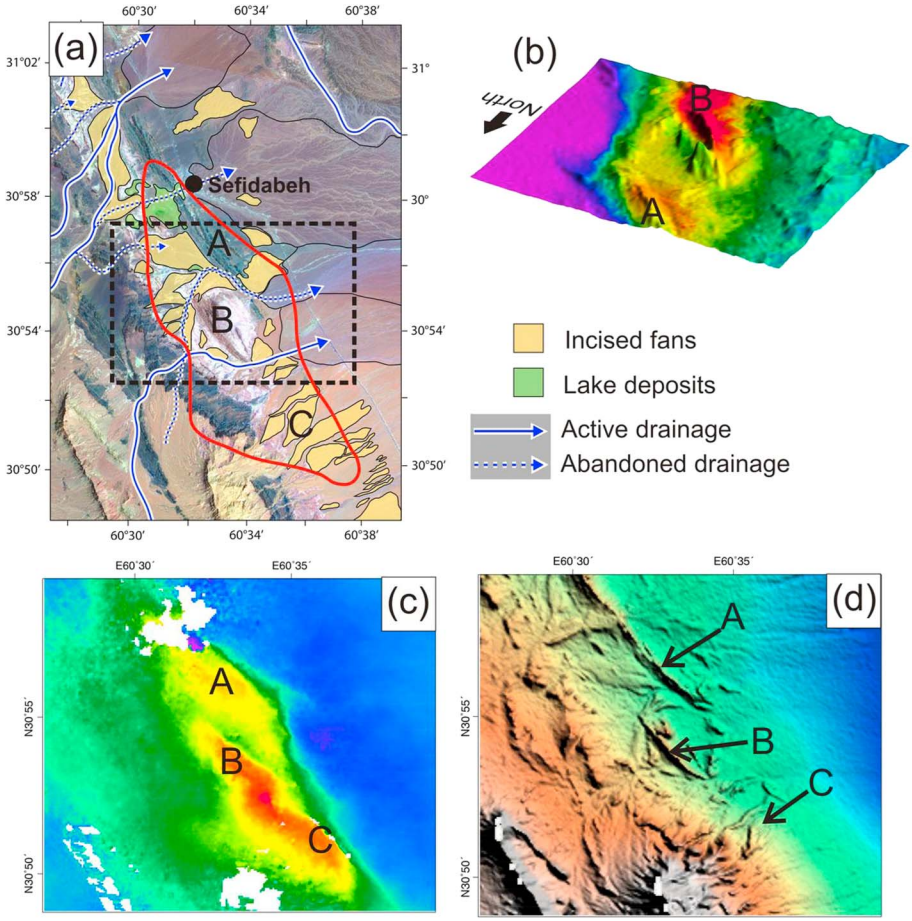

Figure 6. Geomorphology in the region of the Sefidabeh earthquake sequence. (a) Landsat image interpreted with the main geomorphic features (from *Berberian et al.* [2000] and our own interpretations of the landscape). The red line surrounds the area with more than 15 mm LOS postseismic displacements in the InSAR interferogram shown in Figure 4c. (b) The postseismic InSAR interferogram shown in Figure 4c draped over a digital elevation model of the region (illuminated from the right). The area of coverage is shown by the black dashed box in Figure 6a. The total relief in the area shown is ~200 m. (c) The postseismic InSAR displacements shown in Figure 4c. (d) The local topography, illuminated from the NE. The total relief in the area shown is ~750 m. Two ridges are marked as A and B on the figures. Note that these ridges experienced close to the maximum displacement in the postseismic period and in the longer term have uplifted and been responsible for drainage diversions and the uplift and incision of fan surfaces and lake deposits (Figure 6a) [*Berberian et al.*, 2000]. Region "C" also experienced large amounts of postseismic uplift and is a location of pronounced incision of alluvial fans.

6. Discussion

6.1. Geological Controls on Seismic Cycle Behavior

An obvious question raised by the deformation viewed at Sefidabeh is how common is such behavior in thrust belts worldwide? There are plentiful studies of the contrasting behavior of thick sedimentary sequences in which shortening primarily occurs by the pervasive deformation of the sediments and/or bedding plane slip [e.g., *Allmendinger and Shaw*, 2000; *Scharer et al.*, 2006; *Daeron et al.*, 2007; *Charreau et al.*, 2008]. At Sefidabeh, in contrast, the shallow deformation occurred dominantly by slip on a small number of discrete planes. The dips of these planes show that they do not represent bedding planes (which are approximately vertical) [*Berberian et al.*, 2000] but are similar to the 30–50° dips of the coseismic fault planes at depths of 5–10 km [*Berberian et al.*, 2000; *Parsons et al.*, 2006]. We suggest that the difference between the mode of deformation at Sefidabeh and those areas that deform by distributed deformation may be due to the geological histories of the regions. The rocks being actively deformed at Sefidabeh are Cretaceous to Paleogene volcanoclastics, flysch, and limestones, which were deformed in the early Tertiary by a combination of isoclinal folding and faulting [e.g., *Freund*, 1970; *Geological Survey of Iran*, 1991] (Figure 1d). It is likely that they are materially more competent than thick piles of recent (e.g., mid-Miocene and younger)

sediments deposited on range-fronts, such as documented in studies of pervasive fold growth in the Tien Shan and Himalayan forelands and the Los Angeles Basin [e.g., *Allmendinger and Shaw*, 2000; *Scharer et al.*, 2006; *Daeron et al.*, 2007; *Charreau et al.*, 2008]. We suggest this difference in surface geology may be the cause of the contrasting styles of shallow deformation. Only further observations from regions where competent bedrock ranges are undergoing active deformation will reveal how common the style of displacements seen at Sefidabeh may be.

An implication of the shallow deformation at Sefidabeh being distributed on multiple fault strands is that structures within the uplifting hanging walls of the range-bounding faults are currently active (Figure 6). This result has implications for slip rates estimated on range-front structures in this and similar regions. If shallow slip is distributed between the range-front and the interior of the topography, as at Sefidabeh, slip rates estimated for the range-front alone will underestimate the total amount of activity in the fault system as a whole.

6.2. The Timing of Shallow Deformation Within The Seismic Cycle

A general implication of our observations at Sefidabeh is related to the relative timing of deformation at different depths within the crust. Coseismic slip occurred at depths of 5–10 km and postseismic slip from the surface to the base of the seismogenic layer. Similar features have been seen in numerous earthquakes, with coseismic slip either decreasing toward to surface or not reaching the surface [e.g., *Fialko et al.*, 2005, and references therein]. The agreement between the locations of postseismic motion and the indications of uplift preserved in the geomorphology suggests that the geological evolution of the Sefidabeh region is controlled by seismic cycles resulting in the location and style deformation we have imaged. In this case, an examination of the shallow geology accessible to surface observations and boreholes would be studying features produced by postseismic motion, along with any minor coseismic slip that could have occurred and remained invisible to the previous seismological and geodetic studies of the earthquakes [*Berberian et al.*, 2000; *Parsons et al.*, 2006]. Therefore, in regions behaving similar to Sefidabeh, inferences of the properties or stress state of the crust based upon observations of shallow faults may be related to post-seismic deformation in response to deeper coseismic slip, rather than to earthquakes on the observed faults and the wider stress state of the region.

The situation in which the hanging wall of a major thrust fault is broken up by shallow faults has been recognized previously in continental settings [e.g., *Perez-Estaun et al.*, 1988; *Davis et al.*, 1989] and also in seismic images of accretionary wedges above subduction zone megathrusts [e.g., *Park et al.*, 2002]. However, a notable aspect of this study is that it has allowed the timing of motion on such structures at Sefidabeh to be identified and the role they play in the seismic cycle and the evolution of the landscape in the region to be determined. A useful avenue for further work in this regard will be to compare the coseismic and post-seismic motions at Sefidabeh with detailed mapping of the geological structures in the region, in order to establish what proportions of the total deformation could have been produced by the mechanisms that have been observed. However, such work will involve mapping and distinguishing between multiple different generations of deformation and is beyond the scope of the present study.

6.3. Mechanisms of Producing Topography

The results presented above allow us to study the mechanisms by which topography can grow above crustal-scale thrust faults. For a seismic cycle to result in the net production of short-wavelength topography (e.g., kilometer-scale uplifting ridges), there must be an imbalance between interseismic strain accumulation and coseismic and postseismic slip. A cycle of elastic strain accumulation, and its release in an earthquake, on a thrust fault that extends from the surface to the base of the seismogenic layer, would produce topography resembling a step between two gently sloping land surfaces. The wavelength of these gentle slopes will depend upon the elastic thickness, and for realistic values (e.g., $T_e \geq 5$ km), the slopes should extend for tens of kilometers either side of the fault (Figure 7). Such a conceptual model therefore does not explain the presence of narrow topographic features growing above faults. *King et al.* [1988] suggested that the production of short-wavelength topography could be accomplished if the upper crust had an elastic thickness during the interseismic period of less than half of that over which it was able to break in earthquakes. The almost constant thickness of the seismogenic layer throughout the earthquake cycle [e.g., *Rolandone et al.*, 2004] suggests that this mechanism does not operate. Additionally, *King et al.* [1988] neglected the effects of interseismic elastic strain accumulation. An alternative explanation is therefore required.

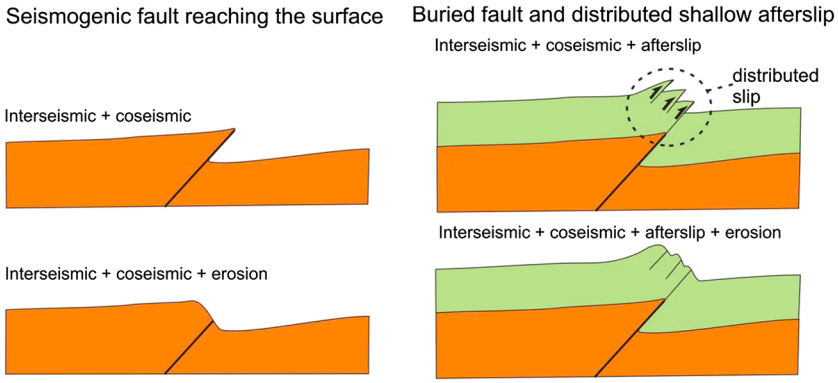

Figure 7. The contrasting topography produced by a seismic cycle with two different configurations of faulting: (left) a fault that slips coseismically and reaches the surface on a single plane and (right) a buried seismogenic fault underlying multiple postseismically creeping shallow faults. Such a configuration produces multiple narrow topographic ridges parallel to the fault, as described for regions A and B in Figure 6.

One possibility is presented by previous work on the growth of folds above thrust faults by the pervasive deformation of sediments in the shallow crust [e.g., *Lavé and Avouac*, 2000; *Allmendinger and Shaw*, 2000; *Scharer et al.*, 2006; *Daeron et al.*, 2007; *Charreau et al.*, 2008], in which cases short-wavelength folds are often produced. At Sefidabeh, in contrast, the earthquakes and postseismic results show that the entire seismogenic layer, to depths of over 10 km, participated in the deformation, and that the shallow deformation was concentrated onto discrete faults rather than being distributed throughout a sedimentary pile. Our observations therefore require an alternative mechanism for the production of topography during the seismic cycle.

At Sefidabeh, the shape and location of the coseismic uplift patch indicates that the dominant location of coseismic slip was on faults that, if projected to the surface, would outcrop near the eastern edge of the ridges visible in the topography, at the junction with the low-lying alluvial fans [*Parsons et al.*, 2006] (Figure 4b). There was postseismic slip on range-front faults that probably represent the continuations of these coseismic fault planes, and also on faults in the interior of the range that break up the coseismic hanging walls. These hanging wall faults are not known to have slipped coseismically and could only have generated minor and shallow slip in order to avoid detection by seismology and InSAR studies of the earthquake sequence [*Berberian et al.*, 2000; *Parsons et al.*, 2006]. Such coseismic slip seems unlikely, as it would need to be separated both laterally and vertically from the main slip patch. Our results from Sefidabeh are not unique: *Donnellan et al.* [2002] observed postseismic hanging wall slip following the 1994 M_w 6.7 Northridge (California) earthquake, and *Ryder et al.* [2010] observed an analogous situation in which the hanging wall of a normal-faulting fault plane in Tibet was broken up by an aftershock and afterslip on a synthetic normal fault. A kinematic model that is consistent with our observations, and with the condition that over an entire seismic cycle the deformation at all depths within the seismogenic layer should be the same, is shown in Figure 7. The shallow slip that must occur to make up the vertical displacement gradient produced by the buried coseismic slip is distributed between multiple fault strands. That some of these strands only slipped at relatively shallow depths is shown by the short-wavelength features in the postseismic interferograms and confirmed by the inversion results. These shallow faults will produce only short-wavelength surface topography. In addition, it appears that these faults are sliding in response to the coseismically induced stress changes, rather than slipping in earthquakes due to accumulated elastic displacement. As such, they may not be accumulating elastic strain at any time, but only sliding in response to externally applied stresses. Such a situation provides a means to "freeze in" short-wavelength topographic, geomorphological, and geological structures; the motions produced by the postseismic slip are not balanced within the footwall and hanging wall by prior elastic strain buildup, as is the case in a standard "elastic rebound" seismic cycle.

7. Conclusions

InSAR observations of the postseismic ground motion following the 1994 Sefidabeh earthquake sequence have demonstrated a mechanism of topographic development above an active thrust fault. Shallow post-

seismic afterslip on an array of faults results in a pattern of uplift that is in agreement with the long-term topographic growth visible in the geomorphology. This afterslip accommodates at least part of the vertical displacement gradient resulting from the buried nature of the coseismic slip. The afterslip is visible for over 16 years following the earthquakes, and the characteristic timescale for relaxation is greater than 4 years. Some of the postseismic fault slip occurred on faults within the hanging walls of the coseismic fault planes and provides a mechanism to develop short-wavelength topographic and geological features in regions of active thrust faulting.

Acknowledgments
The SAR data were provided by the European Space Agency. We thank James Jackson for useful discussions and two anonymous reviewers for comments on the manuscript. This study forms part of the NERC- and ESRC-funded project "Earthquakes without Frontiers."

References

Allmendinger, R. W., and J. H. Shaw (2000), Estimation of fault propagation distance from fold shape: Implications for earthquake hazard assessment, *Geology*, *28*, 1099–1102.

Berberian, M., J. A. Jackson, M. Qorashi, M. Talebian, M. Khatib, and K. Priestley (2000), The 1994 Sefidabeh earthquakes in Eastern Iran: Blind thrust faulting and bedding-plane slip on a growing anticline, and active tectonics of the Sistan suture zone, *Geophys. J. Int.*, *142*, 283–299.

Charreau, J., J.-P. Avouac, Y. Chen, S. Dominguez, and S. Gilder (2008), Miocene to present kinematics of fault-bend folding across the Huerguosi anticline, Northern Tianshan (China), derived from structural, seismic, and magnetostratigraphic data, *Geology*, *36*, 871–874.

Chen, Y.-G., K.-Y. Lai, Y.-H. Lee, J. Suppe, W.-S. Chen, Y.-N. N. Lin, Y. Wang, J.-H. Hung, and Y.-T. Kuo (2007), Coseismic fold scarps and their kinematic behavior in the 1999 Chi-Chi earthquake Taiwan, *J. Geophys. Res.*, *112*, B03S02, doi:10.1029/2006JB004388.

Copley, A. (2014), Postseismic afterslip 30 years after the 1978 Tabas-e-Golshan (Iran) earthquake: Observations and implications for the geological evolution of thrust belts, *Geophys. J. Int.*, doi:10.1093/gji/ggu023.

Copley, A., J.-P. Avouac, J. Hollingsworth, and S. Leprince (2011), The 2001 Mw 7.6 Bhuj earthquake, low fault friction, and the crustal support of plate driving forces in India, *J. Geophys. Res.*, *116*, B08405, doi:10.1029/2010JB008137.

Copley, A., J. Hollingsworth, and E. Bergman (2012), Constraints on fault and lithosphere rheology from the coseismic slip and postseismic afterslip of the 2006 Mw7.0 Mozambique earthquake, *J. Geophys. Res.*, *117*, B03404, doi:10.1029/2011JB008580.

Daeron, M., J.-P. Avouac, and J. Charreau (2007), Modeling the shortening history of a fault tip fold using structural and geomorphic records of deformation, *J. Geophys. Res.*, *112*, B03S13, doi:10.1029/2006JB004460.

D'Agostino, N., D. Cheloni, G. Fornaro, R. Giuliani, and D. Reale (2012), Space-time distribution of afterslip following the 2009 L'Aquila earthquake, *J. Geophys. Res.*, *117*, B02402, doi:10.1029/2011JB008523.

Davis, T. L., J. Namson, and R. F. Yerkes (1989), A cross section of the Los Angeles area: Seismically active fold and thrust belt, the 1987 Whittier Narrows earthquake, and earthquake hazard, *J. Geophys. Res.*, *94*, 9644–9664.

Donnellan, A., J. W. Parker, and G. Peltzer (2002), Combined GPS and InSAR models of postseismic deformation from the Northridge earthquake, *Pure Appl. Geophys.*, *159*, 2261–2270.

Farr, T. G., and M. Kobrick (2000), Shuttle radar topography mission produces a wealth of data, *Eos Trans. AGU*, *81*, 583–585.

Fialko, Y., D. Sandwell, M. Simons, and P. Rosen (2005), Three-dimensional deformation caused by the Bam, Iran, earthquake and the origin of shallow slip deficit, *Nature*, *435*, 295–299.

Fielding, E. J., T. J. Wright, J. Muller, B. E. Parsons, and R. Walker (2004), Aseismic deformation of a fold-and-thrust belt imaged by synthetic aperture radar interferometry near Shahdad, southeast Iran, *Geology*, *32*, 577–580.

Freund, R. (1970), Rotation of strike slip faults in Sistan, southeast Iran, *J. Geol.*, *78*, 188–200.

Geological Survey of Iran (1991), Daryacheh-Ye-Hamun quadrangle map, scale 1:250,000, Geol. Surv. of Iran.

Hsu, Y.-J., M. Simons, J.-P. Avouac, J. Galetzka, K. Sieh, M. Chlieh, D. Natawidjaja, L. Prawirodirdjo, and Y. Bock (2006), Frictional afterslip following the 2005 Nias-Simeulue earthquake, Sumatra, *Science*, *312*, 1921–1926.

Johanson, I. A., and R. Burgmann (2010), Coseismic and postseismic slip from the 2003 San Simeon earthquake and their effects on backthrust slip and the 2004 Parkfield earthquake, *J. Geophys. Res.*, *115*, B07411, doi:10.1029/2009JB006599.

Johnson, K., R. Burgmann, and K. Larson (2006), Frictional properties on the San Andreas Fault near Parkfield, California, inferred from models of afterslip following the 2004 earthquake, *Bull. Seismol. Soc. Amer.*, *96*, S321–S338, doi:10.1785/0120050808.

Johnson, K. M., R. Burgmann, and J. T. Freymueller (2009), Coupled afterslip and viscoelastic flow following the 2002 Denali Fault, Alaska earthquake, *Geophys. J. Int.*, *176*, 670–682.

King, G. C. P., R. S. Stein, and J. B. Rundle (1988), The growth of geological structures by repeated earthquakes 1: Conceptual framework, *J. Geophys. Res.*, *93*, 13,307–13,318.

Lavé, J., and J. P. Avouac (2000), Active folding of fluvial terraces across the Siwaliks Hills, Himalayas of central Nepal, *J. Geophys. Res.*, *105*, 5735–5770.

Lyzenga, G. A., W. R. Panero, and A. Donnellan (2000), Influence of anelastic surface layers on postseismic thrust fault deformation, *J. Geophys. Res.*, *105*, 3151–3157.

Nissen, E., M. Ghorashi, J. Jackson, B. Parsons, and M. Talebian (2007), The 2005 Qeshm Island earthquake (Iran)—A link between buried reverse faulting and surface folding in the Zagros Simply Folded Belt?, *Geophys. J. Int.*, *171*, 326–338.

Okada, Y. (1985), Surface deformation due to shear and tensile faults in a half-space, *Bull. Seismol. Soc. Amer.*, *75*(4), 1135–1154.

Park, J.-O., T. Tsuru, S. Kodaira, P. R. Cummins, and Y. Kaneda (2002), Splay fault branching along the Nankai subduction zone, *Science*, *297*, 1157–1160.

Parsons, B., T. Wright, P. Rowe, J. Andrews, J. Jackson, R. Walker, M. Khatib, M. Talebian, E. Bergman, and E. R. Engdahl (2006), The 1994 Sefidabeh (eastern Iran) earthquakes revisited: New evidence from satellite radar interferometry and carbonate dating about the growth of an active fold above a blind thrust fault, *Geophys. J. Int.*, *164*, 202–217.

Perez-Estaun, A., F. Bastida, J. L. Alonso, J. Marquinez, J. Aller, J. Alvarez-Marron, A. Marcos, and J. A. Pulgar (1988), A thin-skinned tectonics model for an arcuate fold and thrust belt: The Cantabrian zone (Variscan Ibero-Armorican arc), *Tectonics*, *7*, 517–537.

Perfettini, H., and J.-P. Avouac (2004), Postseismic relaxation driven by brittle creep: A possible mechanism to reconcile geodetic measurements and the decay rate of aftershocks, application to the Chi-Chi earthquake, Taiwan, *J. Geophys. Res.*, *109*, B02304, doi:10.1029/2003JB002488.

Philip, H., E. Rogozhin, A. Cisternas, J. C. Bousquet, B. Borisov, and A. Karakhanian (1992), The Armenian earthquake of 1988 December 7: Faulting and folding, neotectonics and palaeoseismicity, *Geophys. J. Int.*, *110*, 141–158.

Rolandone, F., R. Burgmann, and R. M. Nadeau (2004), The evolution of the seismic-aseismic transition during the earthquake cycle: Constraints from the time-dependent depth distribution of aftershocks, *Geophys. Res. Lett.*, *31*, L23610, doi:10.1029/2004GL021379.

Rosen, P. A., S. Hensley, and G. Peltzer (2004), Updates repeat orbit interferometry package released, *Eos Trans. AGU*, *85*(5), 47. [Available at http://www.agu.org/pubs/crossref/2004/2004EO050004.shtml.]

Ryder, I., R. Burgmann, and J. Sun (2010), Tandem afterslip on connected fault planes following the 2008 Nima-Gaize (Tibet) earthquake, *J. Geophys. Res.*, *115*, B03404, doi:10.1029/2009JB006423.

Savage, J. C., J. L. Svarc, and S.-B. Yu (2005), Postseismic relaxation and transient creep, *J. Geophys. Res.*, *110*, B11402, doi:10.1029/2005JB003687.

Scharer, K. M., D. W. Burbank, J. Chen, and R. J. Weldon (2006), Kinematic models of fluvial terraces over active detachment folds: Constraints on the growth mechanism of the Kashi-Atushi fold system, Chinese Tian Shan, *Geol. Soc. Am. Bull.*, *118*, 1006–1021.

Segall, P., R. Burgmann, and M. Matthews (2000), Time-dependent triggered afterslip following the 1989 Loma Prieta earthquake, *J. Geophys. Res.*, *105*, 5615–5634.

Stein, R. S., and G. C. P. King (1984), Seismic potential revealed by surface folding: 1983 Coalinga, California, earthquake, *Science*, *224*, 869–872.

Suito, H., and J. T. Freymueller (2009), A viscoelastic and afterslip postseismic deformation model for the 1964 Alaska earthquake, *J. Geophys. Res.*, *114*, B11404, doi:10.1029/2008JB005954.

Wald, D. J., T. H. Heaton, and K. W. Hudnut (1996), The slip history of the 1994 Northridge, California, earthquake determined from strong-motion, teleseismic, GPS, and leveling data, *Bull. Seismol. Soc. Am.*, *86*, 49–70.

Yielding, G. H., J. A. Jackson, G. C. P. King, H. Sinvhal, C. Vita-Finzi, and R.-M. Wood (1981), Relations between surface deformation, fault geometry, seismicity, and rupture characteristics during the El Asnam (Algeria) earthquake of 10 October 1980, *Earth Planet. Sci. Lett.*, *56*, 287–304.